Wireless Power Transfer via Strongly Coupled Magnetic Resonances

André Kurs,[1]* Aristeidis Karalis,[2] Robert Moffatt,[1] J. D. Joannopoulos,[1]
Peter Fisher,[3] Marin Soljačić[1]

Using self-resonant coils in a strongly coupled regime, we experimentally demonstrated efficient nonradiative power transfer over distances up to 8 times the radius of the coils. We were able to transfer 60 watts with ~40% efficiency over distances in excess of 2 meters. We present a quantitative model describing the power transfer, which matches the experimental results to within 5%. We discuss the practical applicability of this system and suggest directions for further study.

In the early 20th century, before the electrical-wire grid, Nikola Tesla (1) devoted much effort toward schemes to transport power wirelessly. However, typical embodiments (e.g., Tesla coils) involved undesirably large electric fields. The past decade has witnessed a surge in the use of autonomous electronic devices (laptops, cell phones, robots, PDAs, etc.). As a consequence, interest in wireless power has reemerged (2–4). Radiative transfer (5), although perfectly suitable for transferring information, poses a number of difficulties for power transfer applications: The efficiency of power transfer is very low if the radiation is omnidirectional, and unidirectional radiation requires an uninterrupted line of sight and sophisticated tracking mechanisms. A recent theoretical paper (6) presented a detailed analysis of the feasibility of using resonant objects coupled through the tails of their nonradiative fields for midrange energy transfer (7). Intuitively, two resonant objects of the same resonant frequency tend to exchange energy efficiently, while dissipating relatively little energy in extraneous off-resonant objects. In systems of coupled resonances (e.g., acoustic, electromagnetic, magnetic, nuclear), there is often a general "strongly coupled" regime of operation (8). If one can operate in that regime in a given system, the energy transfer is expected to be very efficient. Midrange power transfer implemented in this way can be nearly omnidirectional and efficient, irrespective of the geometry of the surrounding space, with low interference and losses into environmental objects (6).

The above considerations apply irrespective of the physical nature of the resonances. Here, we focus on one particular physical embodiment: magnetic resonances (9). Magnetic resonances are particularly suitable for everyday applications because most of the common materials do not interact with magnetic fields, so interactions with environmental objects are suppressed even further. We were able to identify the strongly coupled regime in the system of two coupled magnetic resonances by exploring nonradiative (near-field) magnetic resonant induction at megahertz frequencies. At first glance, such power transfer is reminiscent of the usual magnetic induction (10); however, note that the usual nonresonant induction is very inefficient for midrange applications.

Overview of the formalism. Efficient midrange power transfer occurs in particular regions of the parameter space describing resonant objects strongly coupled to one another. Using coupled-mode theory to describe this physical system (11), we obtain the following set of linear equations:

$$\dot{a}_m(t) = (i\omega_m - \Gamma_m)a_m(t) + \sum_{n \neq m} i\kappa_{mn}a_n(t) + F_m(t) \qquad (1)$$

where the indices denote the different resonant objects. The variables $a_m(t)$ are defined so that the energy contained in object m is $|a_m(t)|^2$, ω_m is the resonant angular frequency of that isolated object, and Γ_m is its intrinsic decay rate (e.g., due to absorption and radiated losses). In this framework, an uncoupled and undriven oscillator with parameters ω_0 and Γ_0 would evolve in time as $\exp(i\omega_0 t - \Gamma_0 t)$. The $\kappa_{mn} = \kappa_{nm}$ are coupling coefficients between the resonant objects indicated by the subscripts, and $F_m(t)$ are driving terms.

We limit the treatment to the case of two objects, denoted by source and device, such that the source (identified by the subscript S) is driven externally at a constant frequency, and the two objects have a coupling coefficient κ. Work is extracted from the device (subscript D) by means of a load (subscript W) that acts as a circuit resistance connected to the device, and has the effect of contributing an additional term Γ_W to the unloaded device object's decay rate Γ_D. The overall decay rate at the device is therefore $\Gamma_D' = \Gamma_D + \Gamma_W$. The work extracted is determined by the power dissipated in the load, that is, $2\Gamma_W|a_D(t)|^2$. Maximizing the efficiency η of the transfer with respect to the loading Γ_W, given Eq. 1, is equivalent to solving an impedance-matching problem. One finds that the scheme works best when the source and the device are resonant, in which case the efficiency is

$$\eta = \frac{\Gamma_W|a_D|^2}{\Gamma_S|a_S|^2 + (\Gamma_D + \Gamma_W)|a_D|^2}$$

$$= \frac{\frac{\Gamma_W}{\Gamma_D}\frac{\kappa^2}{\Gamma_S\Gamma_D}}{\left[\left(1 + \frac{\Gamma_W}{\Gamma_D}\right)\frac{\kappa^2}{\Gamma_S\Gamma_D}\right] + \left[\left(1 + \frac{\Gamma_W}{\Gamma_D}\right)^2\right]} \qquad (2)$$

The efficiency is maximized when $\Gamma_W/\Gamma_D = [1 + (\kappa^2/\Gamma_S\Gamma_D)]^{1/2}$. It is easy to show that the key to efficient energy transfer is to have $\kappa^2/\Gamma_S\Gamma_D > 1$. This is commonly referred to as the strong coupling regime. Resonance plays an essential role in this power transfer mechanism, as the efficiency is improved by approximately ω^2/Γ_D^2 (~10^6 for typical parameters) relative to the case of inductively coupled nonresonant objects.

Theoretical model for self-resonant coils. Our experimental realization of the scheme consists of two self-resonant coils. One coil (the source coil) is coupled inductively to an oscillating circuit; the other (the device coil) is coupled inductively to a resistive load (12) (Fig. 1). Self-resonant coils rely on the interplay between distributed inductance and distributed capacitance to achieve resonance. The coils are made of an electrically conducting wire of total length l and cross-sectional radius a wound into a helix of n turns, radius r, and height h. To the best of our knowledge, there is no exact solution for a finite helix in the literature, and even in the case of infinitely long coils, the solutions rely on assumptions that are inadequate for our system (13). We have found, however, that the simple quasi-static model described below is in good agreement (within ~5%) with experiment.

We start by observing that the current must be zero at the ends of the coil, and we make the educated guess that the resonant modes of the coil are well approximated by sinusoidal current profiles along the length of the conducting wire. We are interested in the lowest mode, so if we denote by s the parameterization coordinate along the length of the conductor, such that it runs from $-l/2$ to $+l/2$, then the time-dependent current profile has the form $I_0 \cos(\pi s/l) \exp(i\omega t)$. It follows from the continuity equation for charge that the linear charge density profile is of the form $\lambda_0 \sin(\pi s/l) \exp(i\omega t)$, so that one-half of the coil (when sliced perpendicularly to its axis) contains an oscillating total charge (of amplitude $q_0 = \lambda_0 l/\pi$) that is equal in magnitude but opposite in sign to the charge in the other half.

As the coil is resonant, the current and charge density profiles are $\pi/2$ out of phase from each

other, meaning that the real part of one is maximum when the real part of the other is zero. Equivalently, the energy contained in the coil is at certain points in time completely due to the current, and at other points it is completely due to the charge. Using electromagnetic theory, we can define an effective inductance L and an effective capacitance C for each coil as follows:

$$L = \frac{\mu_0}{4\pi|I_0|^2} \iint d\mathbf{r} d\mathbf{r}' \frac{\mathbf{J}(\mathbf{r}) \cdot \mathbf{J}(\mathbf{r}')}{|\mathbf{r} - \mathbf{r}'|} \qquad (3)$$

$$\frac{1}{C} = \frac{1}{4\pi\varepsilon_0|q_0|^2} \iint d\mathbf{r} d\mathbf{r}' \frac{\rho(\mathbf{r})\rho(\mathbf{r}')}{|\mathbf{r} - \mathbf{r}'|} \qquad (4)$$

where the spatial current $\mathbf{J}(\mathbf{r})$ and charge density $\rho(\mathbf{r})$ are obtained respectively from the current and charge densities along the isolated coil, in conjunction with the geometry of the object. As defined, L and C have the property that the energy U contained in the coil is given by

$$U = \frac{1}{2}L|I_0|^2$$
$$= \frac{1}{2C}|q_0|^2 \qquad (5)$$

Given this relation and the equation of continuity, the resulting resonant frequency is $f_0 = 1/[2\pi(LC)^{1/2}]$. We can now treat this coil as a standard oscillator in coupled-mode theory by defining $a(t) = [(L/2)^{1/2}]I_0(t)$.
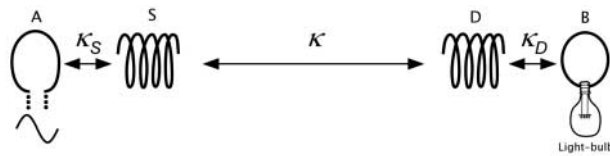
We can estimate the power dissipated by noting that the sinusoidal profile of the current distribution implies that the spatial average of the peak current squared is $|I_0|^2/2$. For a coil with n turns and made of a material with conductivity σ, we modify the standard formulas for ohmic (R_o) and radiation (R_r) resistance accordingly:

$$R_o = \sqrt{\frac{\mu_0\omega}{2\sigma}} \frac{l}{4\pi a} \qquad (6)$$

$$R_r = \sqrt{\frac{\mu_0}{\varepsilon_0}} \left[\frac{\pi}{12} n^2 \left(\frac{\omega r}{c}\right)^4 + \frac{2}{3\pi^3} \left(\frac{\omega h}{c}\right)^2\right] \qquad (7)$$

The first term in Eq. 7 is a magnetic dipole radiation term (assuming $r \ll 2\pi c/\omega$, where c is the speed of light); the second term is due to the electric dipole of the coil and is smaller than

the first term for our experimental parameters. The coupled-mode theory decay constant for the coil is therefore $\Gamma = (R_o + R_r)/2L$, and its quality factor is $Q = \omega/2\Gamma$.

We find the coupling coefficient κ_{DS} by looking at the power transferred from the source to the device coil, assuming a steady-state solution in which currents and charge densities vary in time as $\exp(i\omega t)$:

$$P_{DS} = \int d\mathbf{r} \mathbf{E}_S(\mathbf{r}) \cdot \mathbf{J}_D(\mathbf{r})$$

$$= -\int d\mathbf{r} [\dot{\mathbf{A}}_S(\mathbf{r}) + \nabla\phi_S(\mathbf{r})] \cdot \mathbf{J}_D(\mathbf{r})$$

$$= -\frac{1}{4\pi} \iint d\mathbf{r} d\mathbf{r}'$$

$$\times \left[\mu_0 \frac{\dot{\mathbf{J}}_S(\mathbf{r}')}{|\mathbf{r}' - \mathbf{r}|} + \frac{\rho_S(\mathbf{r}')}{\varepsilon_0} \frac{\mathbf{r}' - \mathbf{r}}{|\mathbf{r}' - \mathbf{r}|^3}\right] \cdot \mathbf{J}_D(\mathbf{r}')$$

$$\equiv -i\omega M I_S I_D \qquad (8)$$

Where M is the effective mutual inductance, ϕ is the scalar potential, $\mathbf{A}$ is the vector potential, and the subscript S indicates that the electric field is due to the source. We then conclude from standard coupled-mode theory arguments that $\kappa_{DS} = \kappa_{SD} = \kappa = \omega M/[2(L_S L_D)^{1/2}]$. When the distance D between the centers of the coils is much larger than their characteristic size, κ scales with the D^{-3} dependence characteristic of dipole-dipole coupling. Both κ and Γ are functions of the frequency, and κ/Γ and the efficiency are maximized for a particular value of f, which is in the range 1 to 50 MHz for typical parameters of interest. Thus, picking an appropriate frequency for a given coil size, as we do in this experimental demonstration, plays a major role in optimizing the power transfer.

Comparison with experimentally determined parameters. The parameters for the two identical helical coils built for the experimental validation of the power transfer scheme are $h = 20$ cm, $a = 3$ mm, $r = 30$ cm, and $n = 5.25$. Both coils are made of copper. The spacing between loops of the helix is not uniform, and we encapsulate the uncertainty about their uniformity by attributing a 10% (2 cm) uncertainty to h. The expected resonant frequency given these dimensions is $f_0 = 10.56 \pm 0.3$ MHz, which is

about 5% off from the measured resonance at 9.90 MHz.

The theoretical Q for the loops is estimated to be ~2500 (assuming $\sigma = 5.9 \times 10^7$ m/ohm), but the measured value is $Q = 950 \pm 50$. We believe the discrepancy is mostly due to the effect of the layer of poorly conducting copper oxide on the surface of the copper wire, to which the current is confined by the short skin depth (~20 μm) at this frequency. We therefore use the experimentally observed Q and $\Gamma_S = \Gamma_D = \Gamma = \omega/2Q$ derived from it in all subsequent computations.

We find the coupling coefficient κ experimentally by placing the two self-resonant coils (fine-tuned, by slightly adjusting h, to the same resonant frequency when isolated) a distance D apart and measuring the splitting in the frequencies of the two resonant modes. According to coupled-mode theory, this splitting should be $\Delta\omega = 2[(\kappa^2 - \Gamma^2)^{1/2}]$. In the present work, we focus on the case where the two coils are aligned coaxially (Fig. 2), although similar results are obtained for other orientations (figs. S1 and S2).

Measurement of the efficiency. The maximum theoretical efficiency depends only on the parameter $\kappa/[(L_S L_D)^{1/2}] = \kappa/\Gamma$, which is greater than 1 even for $D = 2.4$ m (8 times the radius of the coils) (Fig. 3). Thus, we operate in the strongly coupled regime throughout the entire range of distances probed.

As our driving circuit, we use a standard Colpitts oscillator whose inductive element consists of a single loop of copper wire 25 cm in radius (Fig. 1); this loop of wire couples inductively to the source coil and drives the entire wireless power transfer apparatus. The load consists of a calibrated light bulb (14) and is attached to its own loop of insulated wire, which is placed in proximity of the device coil and inductively coupled to it. By varying the distance between the light bulb and the device coil, we are able to adjust the parameter Γ_W/Γ so that it matches its optimal value, given theoretically by $[1 + (\kappa^2/\Gamma^2)]^{1/2}$. (The loop connected to the
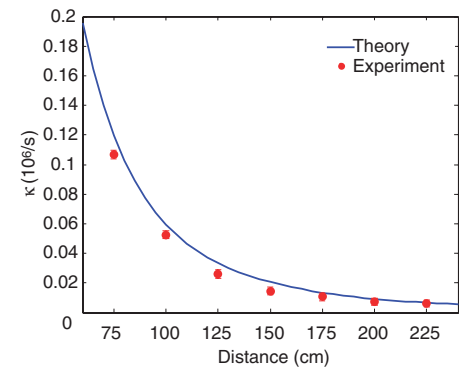

Fig. 2. Comparison of experimental and theoretical values for κ as a function of the separation between coaxially aligned source and device coils (the wireless power transfer distance).

Fig. 1. Schematic of the experimental setup. A is a single copper loop of radius 25 cm that is part of the driving circuit, which outputs a sine wave with frequency 9.9 MHz. S and D are respectively the source and device coils referred to in the text. B is a loop of wire attached to the load (light bulb). The various κs represent direct couplings between the objects indicated by the arrows. The angle between coil D and the loop A is adjusted to ensure that their direct coupling is zero. Coils S and D are aligned coaxially. The direct couplings between B and A and between B and S are negligible.

light bulb adds a small reactive component to Γ_W, which is compensated for by slightly retuning the coil.) We measure the work extracted by adjusting the power going into the Colpitts oscillator until the light bulb at the load glows at its full nominal brightness.

We determine the efficiency of the transfer taking place between the source coil and the load by measuring the current at the midpoint of each of the self-resonant coils with a current probe (which does not lower the Q of the coils noticeably). This gives a measurement of the current parameters I_S and I_D used in our theoretical model. We then compute the power dissipated in each coil from $P_{S,D} = \Gamma L |I_{S,D}|^2$, and obtain the efficiency from $\eta = P_W/(P_S + P_D + P_W)$. To ensure that the experimental setup is well described by a two-object coupled mode theory model, we position the device coil such that its direct coupling to the copper loop attached to the Colpitts oscillator is zero. The experimental results are shown in Fig. 4, along with the theoretical prediction for maximum efficiency, given by Eq. 2. We were able to transfer several tens of watts with the use of this setup, fully lighting up a 60-W light bulb from distances more than 2 m away (figs. S3 and S4).

As a cross-check, we also measured the total power going from the wall power outlet into the driving circuit. The efficiency of the wireless transfer itself is hard to estimate in this way, however, as the efficiency of the Colpitts oscillator itself is not precisely known, although it is expected to be far from 100% (15). Still, the ratio of power extracted to power entering the driving circuit gives a lower bound on the efficiency. When transferring 60 W to the load over a distance of 2 m, for example, the power flowing into the driving circuit is 400 W. This yields an overall wall-to-load efficiency of 15%, which is reasonable given the expected efficiency of 40 to 50% for the wireless power trans-
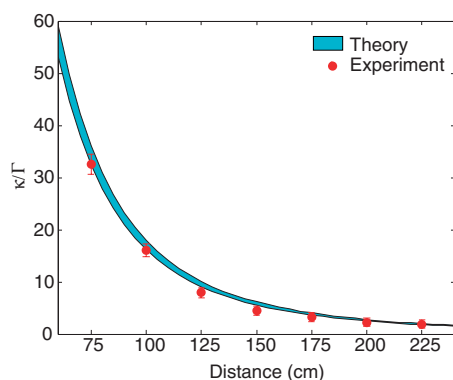
fer at that distance and the low efficiency of the Colpitts oscillator.

Concluding remarks. It is essential that the coils be on resonance for the power transfer to be practical (6). We find experimentally that the power transmitted to the load drops sharply as either one of the coils is detuned from resonance. For a fractional detuning $\Delta f/f_0$ of a few times the inverse loaded Q, the induced current in the device coil is indistinguishable from noise.

A detailed and quantitative analysis of the effect of external objects on our scheme is beyond the scope of this work, but we note here that the power transfer is not visibly affected as humans and various everyday objects, such as metals, wood, and electronic devices large and small, are placed between the two coils—even in cases where they completely obstruct the line of sight between source and device (figs. S3 to S5). External objects have a noticeable effect only when they are within a few centimeters from either one of the coils. Some materials (such as aluminum foil, Styrofoam, and humans) mostly just shift the resonant frequency, which can in principle be easily corrected with a feedback circuit; other materials (cardboard, wood, and polyvinyl chloride) lower Q when placed closer than a few centimeters from the coil, thereby lowering the efficiency of the transfer.

When transferring 60 W across 2 m, we calculate that at the point halfway between the coils, the root mean square (RMS) magnitude of the electric field is $E_{RMS} = 210$ V/m, that of the magnetic field is $H_{RMS} = 1$ A/m, and that of the Poynting vector is $S_{RMS} = 3.2$ mW/cm^2 (16). These values increase closer to the coils, where the fields at source and device are comparable. For example, at distances 20 cm away from the
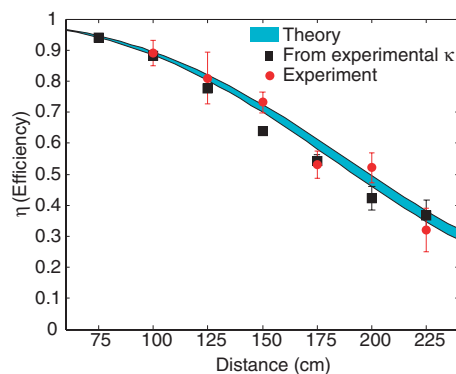
surface of the device coil, we calculate the maximum values for the fields to be $E_{RMS} = 1.4$ kV/m, $H_{RMS} = 8$ A/m, and $S_{RMS} = 0.2$ W/cm^2. The power radiated for these parameters is ~5 W, which is roughly an order of magnitude higher than cell phones. In the particular geometry that we studied, the overwhelming contribution (by one to two orders of magnitude) to the electric near-field, and hence to the near-field Poynting vector, comes from the electric dipole moment of the coils. If instead one uses a capacitively loaded single-turn loop design (6)—which has the advantage of confining nearly all of the electric field inside the capacitor—and tailors the system to operate at lower frequencies, our calculations show (17) that it should be possible to reduce the values cited above for the electric and magnetic fields, the Poynting vector, and the power radiated so that they fall below thresholds specified by general safety regulations [e.g., the IEEE safety standards for general public exposure (18)].

Although the two coils are currently of identical dimensions, it is possible to make the device coil small enough to fit into portable devices without decreasing the efficiency. One could, for instance, maintain the product of the characteristic sizes of the source and device coils constant, as argued in (6).

We believe that the efficiency of the scheme and the power transfer distances could be appreciably improved by silver-plating the coils, which should increase their Q, or by working with more elaborate geometries for the resonant objects (19). Nonetheless, the performance characteristics of the system presented here are already at levels where they could be useful in practical applications.

Fig. 4. Comparison of experimental and theoretical efficiencies as functions of the wireless power transfer distance. The shaded area represents the theoretical prediction for maximum efficiency and is obtained by inserting the theoretical values from Fig. 3 into Eq. 2, with $\Gamma_W/\Gamma_D = [1 + (\kappa^2/\Gamma^2)]^{1/2}$. The black squares are the maximum efficiency obtained from Eq. 2 and experimental values of κ/Γ from Fig. 3. The red dots present the directly measured efficiency, as described in the text.

Fig. 3. Comparison of experimental and theoretical values for the parameter κ/Γ as a function of the wireless power transfer distance. The theory values are obtained by using the theoretical κ and the experimentally measured Γ. The shaded area represents the spread in the theoretical κ/Γ due to the 5% uncertainty in Q.

References and Notes
1. N. Tesla, U.S. patent 1,119,732 (1914).
2. J. M. Fernandez, J. A. Borras, U.S. patent 6,184,651 (2001).
3. A. Esser, H.-C. Skudelny, *IEEE Trans. Ind. Appl.* **27**, 872 (1991).
4. J. Hirai, T.-W. Kim, A. Kawamura, *IEEE Trans. Power Electron.* **15**, 21 (2000).
5. T. A. Vanderelli, J. G. Shearer, J. R. Shearer, U.S. patent 7,027,311 (2006).
6. A. Karalis, J. D. Joannopoulos, M. Soljačić, *Ann. Phys.*, 10.1016/j.aop.2007.04.017 (2007).
7. Here, by midrange, we mean that the sizes of the devices that participate in the power transfer are smaller than the distance between devices by a factor of at least 2 to 3. For example, if the device being powered is a laptop (size ~50 cm) and the power source (size ~50 cm) is in the same room as the laptop, the distance of power transfer could be within a room or a factory pavilion (size on the order of a few meters).
8. T. Aoki *et al.*, *Nature* **443**, 671 (2006).
9. K. O'Brien, G. Scheible, H. Gueldner, in *IECON '03, 29th Annual Conference of the IEEE* (http://ieeexplore.ieee.org/xpl/RecentCon.jsp?punumber=9011) (2003).
10. L. Ka-Lai, J. W. Hay, P. G. W. Beart, U.S. patent 7,042,196 (2006).
11. H. Haus, *Waves and Fields in Optoelectronics* (Prentice-Hall, Englewood Cliffs, NJ, 1984).
12. The couplings to the driving circuit and the load do not have to be inductive. They may also be connected by a wire, for example. We have chosen inductive coupling in the present work because of its easier implementation.
13. S. Sensiper, thesis, Massachusetts Institute of Technology (1951).

14. We experimented with various power ratings from 5 to 75 W.
15. W. A. Edson, *Vacuum-Tube Oscillators* (Wiley, New York, 1953).
16. Note that $E \neq c\mu_0 H$, and that the fields are out of phase and not necessarily perpendicular because we are not in a radiative regime.
17. See supporting material on *Science* Online.
18. *IEEE Std C95.1—2005 IEEE Standard for Safety Levels with Respect to Human Exposure to Radio Frequency Electromagnetic Fields, 3 kHz to 300 GHz* (IEEE, Piscataway, NJ, 2006).
19. J. B. Pendry, *Science* **306**, 1353 (2004).
20. We thank J. Pendry for suggesting the use of magnetic resonances and M. Grossman and I. Čelanović for technical assistance. Supported by NSF Materials Research Science and Engineering Center grant DMR 02-13282, U.S. Department of Energy grant DE-FG02-99ER45778, and the Army Research Office through the Institute for Soldier Nanotechnologies under contract DAAD-19-02-D0002.

Sea Anemone Genome Reveals Ancestral Eumetazoan Gene Repertoire and Genomic Organization

Nicholas H. Putnam,[1] Mansi Srivastava,[2] Uffe Hellsten,[1] Bill Dirks,[2] Jarrod Chapman,[1] Asaf Salamov,[1] Astrid Terry,[1] Harris Shapiro,[1] Erika Lindquist,[1] Vladimir V. Kapitonov,[3] Jerzy Jurka,[3] Grigory Genikhovich,[4] Igor V. Grigoriev,[1] Susan M. Lucas,[1] Robert E. Steele,[5] John R. Finnerty,[6] Ulrich Technau,[4] Mark Q. Martindale,[7] Daniel S. Rokhsar[1,2]*

Sea anemones are seemingly primitive animals that, along with corals, jellyfish, and hydras, constitute the oldest eumetazoan phylum, the Cnidaria. Here, we report a comparative analysis of the draft genome of an emerging cnidarian model, the starlet sea anemone *Nematostella vectensis*. The sea anemone genome is complex, with a gene repertoire, exon-intron structure, and large-scale gene linkage more similar to vertebrates than to flies or nematodes, implying that the genome of the eumetazoan ancestor was similarly complex. Nearly one-fifth of the inferred genes of the ancestor are eumetazoan novelties, which are enriched for animal functions like cell signaling, adhesion, and synaptic transmission. Analysis of diverse pathways suggests that these gene "inventions" along the lineage leading to animals were likely already well integrated with preexisting eukaryotic genes in the eumetazoan progenitor.

All living tissue-grade animals, or eumetazoans, are descended from the last common ancestor of bilaterians (flies, worms, snails, and humans), cnidarians (anemones, jellyfish, and hydra), and ctenophores (comb jellies) (*1*, *2*). This eumetazoan ancestor lived perhaps 700 million years ago. Although it is not preserved in the fossil record (*3*), we can infer many of its characteristics—flagellated sperm, development through a process of gastrulation, multiple germ layers, true epithelia lying upon a basement membrane, a lined gut (enteron), a neuromuscular system, multiple sensory systems, and fixed body axes—because these conserved features are retained by its modern descendants.

Similarly, we can characterize the genome of this long-extinct eumetazoan progenitor by comparing modern DNA and protein sequences and identifying conserved ancestral features that have an intrinsically slow rate of change and/or are preserved by selective pressures. Comparisons (*4–6*) between fruit fly, nematode, and vertebrate genomes reveal greater genomic complexity in the vertebrates [and other deuterostomes (*7*, *8*)] as measured by gene content and structure, but at the same time show that many genes and networks are shared across bilaterians. Probing the ancestral eumetazoan genome requires sequences from even deeper branches of the animal tree, comparing bilaterian and nonbilaterian phyla.

In comparison with bilaterians, cnidarians appear morphologically simple. The phylum is defined (*2*) by a sac-like body plan with a single oral opening, two epithelial tissue layers, the presence of numerous tentacles, a nerve net, and the characteristic stinging cells (cnidocytes, literally translated as "nettle cells") that give the phylum its name (fig. S1.1G). The class Anthozoa ("flower animals") includes diverse anemones, corals, and sea pens, all of which lack a medusa stage. The other cnidarian classes are united by their pelagic medusae and characteristically linear mitochondrial genomes (*9*) into the Medusozoa, including *Hydra* and related hydroids, jellyfish, and box jellies. The disparate bilaterian phyla of the early Cambrian suggest a Precambrian divergence of the cnidarian lineage from the bilaterian stem, and indeed some of the oldest animal body and embryo fossils are plausibly relics of stem cnidarians [reviewed in (*10*, *11*)].

Among Anthozoan cnidarians, the starlet sea anemone *Nematostella vectensis* is an emerging model system (*12*, *13*). This estuarine burrowing anemone is found on the Atlantic and Pacific coasts of North America, as well as the coast of southeast England (*14*). *Nematostella* cultures are easily maintained in the laboratory; with separate sexes, inducible spawning, and external fertilization (*12*, *15*), embryos are available throughout the year.

Although cnidarians are often characterized as simple or primitive, closer study of *Nematostella* and its relatives has revealed considerable molecular (*16–19*) and morphological complexity (*13*). Based on expressed sequence tag (EST) analyses (*17*, *18*) and the targeted study of specific gene families [reviewed in (*13*, *16*, *20–22*)], signaling pathways and transcription factors involved in the early patterning and development of bilaterians are present in cnidarian genomes and are active in development (*13*, *23–28*), indicating that these pathways and regulatory mechanisms predate the eumetazoan radiation. Perhaps most notably, genes that establish the main body axes in bilaterian embryos are also expressed asymmetrically in *Nematostella* development, even though cnidarians are conventionally viewed as radial animals [for a critical discussion, see (*29*)].

Here, we report the draft genome of the starlet sea anemone and use its gene repertoire and genome organization to reconstruct features of the ancestral eumetazoan genome. Analysis of the *Nematostella* genome in the context of sequences from other eukaryotes reveals the genomic complexity of this last common cnidarian-bilaterian ancestor. The emerging picture from the genome and EST studies (*17*, *18*) is one of extensive conservation in gene content, structure, and organization between *Nematostella* and vertebrates. We show that even chromosome-scale linkage has been preserved between *Nematostella* and vertebrates. These are the most ancient conserved linkages known outside of prokaryotic operons. In contrast, the fruit fly and nematode model systems have experienced extensive gene loss (*18*), intron loss (*30*), and genome rearrangement. Thus, from a genomic perspective, the eumetazoan ancestor more closely resembled modern vertebrates and sea anemones.

Nematostella Genome Assembly and Gene Set

The draft sequence of the *Nematostella* genome was produced with the use of a random shotgun

[1]Department of Energy Joint Genome Institute, Walnut Creek, CA 94598, USA. [2]Center for Integrative Genomics and Department of Molecular and Cell Biology, University of California, Berkeley, CA 94720, USA. [3]Genetic Information Research Institute, 1925 Landings Drive, Mountain View, CA 94043, USA. [4]Sars International Centre for Marine Molecular Biology, University of Bergen, Thormøhlensgt 55, 5008, Bergen, Norway. [5]Department of Biological Chemistry and the Developmental Biology Center, University of California, Irvine, CA 92697, USA. [6]Department of Biology, Boston University, Boston, MA 02215, USA. [7]Kewalo Marine Laboratory, University of Hawaii, Honolulu, HI 96813, USA.

*To whom correspondence should be addressed. E-mail: dsrokhsar@lbl.gov